# A Discrete Geometric Approach to Cell Membrane and Electrode Contact Impedance Modeling

Antonio Affanni, Ruben Specogna*, *Member, IEEE*, and Francesco Trevisan

***Abstract*—This paper presents a novel discrete model for cell membranes and electrodes contact impedances alternative to the widely used finite elements. The finite element approach can be considered as a tool for constructing finite dimensional systems of equations that approximate the specific electroquasistatic biological problem on the discrete level. Although the finite element technique is explained typically in terms of variational or weighted-residual approaches, another, less familiar way is available to reformulate *geometrically* the same physical problem. This approach, referred to as discrete geometric approach, allows a direct link between geometry and the degrees of freedom describing the specific biological problem. It is straightforward to implement in any finite element open software and it assures a correct modeling of voltages and currents playing a fundamental role in a biological problem. The validation has been performed, as a first step, against analytical solutions; then, we considered impedance measurements regarding erythrocytes in whole blood flowing in microchannels at high shear rates.**

***Index Terms*—Cell membrane modeling, complete electrical impedance tomography (EIT) model, contact impedance modeling, discrete geometric approach (DGA), thin layers.**

## I. Introduction

THERE is a great research interest in developing techniques to transport materials into cells through their membranes without damage for the cells and with a precise control over how much material is delivered. A promising technique, often referred to as nanoelectroporation [1], is based on the application of a local electric field to an area one-hundredth the size of those used in microfluidic-based methods. The application of a precise local electric field to the cell membrane induces a transmembrane potential (TMP) distribution on it, which causes permeabilization. Thence, the volume of material delivered to cells can be controlled through a precise voltage distribution along the cell membrane and its time evolution.

In order to evaluate such TMP potentials, the problem of modeling in an accurate way the cell membrane is becoming of increasing interest in bioelectromagnetics research [2], [3]. This is due to the fact that the membrane thickness is orders of magnitudes thinner than the cell size, and trying to produce a volumetric mesh for the membrane is not appealing for various reasons. It is clear, in fact, that a huge number of elements is needed in order to obtain good-shaped tetrahedra (i.e., as close as possible to a regular tetrahedron) in the membrane volume, yielding to an excessive cardinality of mesh elements. Moreover, if the cell shape is complicated, it is also difficult to produce a membrane volume with a uniform thickness [2]. Even though the volumetric meshing of the membrane is frequently performed, see for example [4], [5], a more appealing solution employing thin layers has been introduced in [2]; however, the solution is obtained by applying an appropriate boundary condition in the COMSOL commercial software instead of providing a physical modeling of the membrane layer. A further critical point is the modeling of the electrical interfaces between biological fluids and electrodes.

Therefore, the aim of this paper is twofold. From the one hand, we propose an alternative approach to thin structures modeling. The approach is based on formulating the electromagnetic laws of the electroquasistatic (EQS) regime, directly in a discrete form on a pair of oriented and staggered cell complexes, one dual of the other, leading to the so-called discrete geometric approach (DGA) for computational physics [6], [7]. This approach is attractive because it is straightforward to implement in any open source finite element software and it offers some advantages when a nonlinear or anisotropic conductivity of the membrane is considered.

On the other hand, we will model a general and efficient way, by means of the DGA, the electrodes and external circuits used to apply voltages and currents to the biological tissue under study. This modeling is particularly useful to account for the contact impedance in the case of electrical interfaces with a biological fluid like whole blood flowing in artificial microchannels.

This paper is structured as follows. In Section II, we recall the DGA formulation for 3-D EQS problems. Section III addresses the modeling of the membrane as a thin layer, whereas Section IV describes in detail how to impose boundary conditions and take into account the contact impedance of the electrodes. In Section V, some numerical results are presented for model validation and, in Section VI, the conclusions are drawn.

## II. Electroquasistatic Geometric Formulation

We assume that the computational domain $D$ is a connected subset of the 3-D Euclidean space. We cover $D$ with a simplicial *cell complex* $\mathcal{K}$ whose oriented geometrical elements are nodes $n$, edges $e$, faces $f$ (triangles), and volumes $v$ (tetrahedra) [see Fig. 1(a)]; the cardinality of each geometrical elements set is

Manuscript received April 3, 2012; revised June 14, 2012; accepted July 3, 2012. Date of publication July 11, 2012; date of current version August 16, 2012. This work was supported in part by the Italian Ministry of Education, University and Research (MIUR) under Project PRIN 2009LTRYRE. *Asterisk indicates corresponding author*.

A. Affanni and F. Trevisan are with the Dipartimento di Ingegneria Elettrica, Gestionale e Meccanica, Universita di Udine, Udine 33100, Italy (e-mail: antonio.affanni@uniud.it; trevisan@uniud.it).

*R. Specogna is with the Dipartimento di Ingegneria Elettrica, Gestionale e Meccanica, Universita di Udine, Udine 33100, Italy (e-mail: ruben.specogna@uniud.it).

Color versions of one or more of the figures in this paper are available online at http://ieeexplore.ieee.org.

Digital Object Identifier 10.1109/TBME.2012.2207897

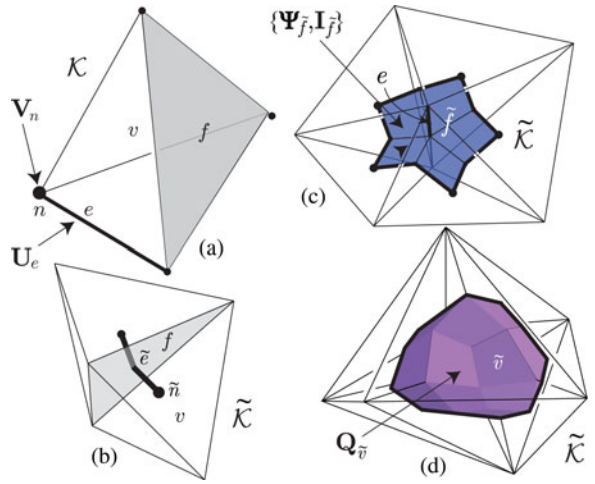


Fig. 1. Geometric elements of $\mathcal{K}$ and $\tilde{\mathcal{K}}$ and their association with physical variables. (a) Geometric elements of $\mathcal{K}$: Nodes $n$, edges $e$, faces $f$ (triangles), and volumes $v$ (tetrahedra). (b) Dual node $\tilde{n}$ is the barycenter of the tetrahedron $v$, a dual edge $\tilde{e}$ is a broken segment of line joining the barycenters of a pair of tetrahedra through the barycenter of the face $f$ they have in common. (c) For each edge $e \in \mathcal{K}$, exists a dual face $\tilde{f}$ bounded by dual edges that are dual to the star of faces incident to $e$. The dual face consists in the union of planar quadrangles, one for each tetrahedron that is incident to the edge $e$. Each quadrangle has one corner in the middle point of the edge, one in the barycenter of a tetrahedron $v$, the other two in the barycenters of the two triangles in the boundary of $v$ that have the edge $e$ in their boundaries. (d) For each node $n \in \mathcal{K}$, exists a dual volume $\tilde{v}$ bounded by dual faces that are dual to the star of edges incident to the node $n$.

denoted as $N$, $E$, $F$, and $V$, respectively. The topology of $\mathcal{K}$ is encoded in the incidence matrices: $\mathbf{G}$ (between the orientations of the pairs $e$ and $n$), $\mathbf{C}$ (between the orientations of the pairs $f$ and $e$), and $\mathbf{D}$ (between the orientations of the pairs $v$ and $f$), see for example [6], [8]. Next, a dual barycentric complex $\tilde{\mathcal{K}}$ is constructed from $\mathcal{K}$ by using the *barycentric subdivision* [8], [9] yielding dual volumes $\tilde{v}$ dual faces $\tilde{f}$, dual edges $\tilde{e}$, and dual nodes $\tilde{n}$ which are in a one to one correspondence (duality) with the geometrical elements $n$, $e$, $f$, and $v$ of $\mathcal{K}$, respectively [see Fig. 1(b)–(d)]. Thanks to the duality between $\mathcal{K}$ and $\tilde{\mathcal{K}}$, the incidence matrices of $\tilde{\mathcal{K}}$ are deduced from those of $\mathcal{K}$ as: $\tilde{\mathbf{G}} = \mathbf{D}^T$, $\tilde{\mathbf{C}} = \mathbf{C}^T$, and $\tilde{\mathbf{D}} = -\mathbf{G}^T$ [8], Sec. 3].

We consider the integrals of the field quantities, the electric field[1] E, the electric displacement field D, the current density vector J, and the charge density scalar field $\rho$ involved in the EQS problem with respect to the oriented geometric elements of $\mathcal{K}$, $\tilde{\mathcal{K}}$, yielding integral variables grouped into degrees of freedom (DoF) arrays [7]. In particular, we denote with $\mathbf{U}$ the array[2] of voltages $\mathbf{U}_e = \int_e \mathrm{E} \cdot d\mathrm{l}$ associated with primal edges $e \in \mathcal{K}$, with $\mathbf{V}$ the array of scalar potentials $\mathbf{V}_n$ associated with primal nodes $n \in \mathcal{K}$; on the dual side, we introduce the array $\mathbf{Q}$ of electric charges $\mathbf{Q}_{\tilde{v}} = \int_{\tilde{v}} \rho dv$ associated with dual volumes $\tilde{v} \in \tilde{\mathcal{K}}$ and the arrays $\mathbf{I}$, $\mathbf{\Psi}$ of electric currents $\mathbf{I}_{\tilde{f}} = \int_{\tilde{f}} \mathrm{J} \cdot d\mathrm{s}$, and electric fluxes $\mathbf{\Psi}_{\tilde{f}} = \int_{\tilde{f}} \mathrm{D} \cdot d\mathrm{s}$ across dual faces $\tilde{f} \in \tilde{\mathcal{K}}$, respectively, Fig. 1. In the following, we will focus on the EQS problem formulated at the angular frequency $\omega$; thence, the DoFs arrays considered are arrays of complex numbers.

According to the DGA, physical laws can be expressed by means of *exact* algebraic relations between the DoFs, using only the topology of the mesh represented by incidence matrices. Faraday's law, in the discrete setting, translates into $\mathbf{CU} = \mathbf{0}$. This algebraic relation is enforced by using the array of electric scalar potentials $\mathbf{V}$ such that

$$\mathbf{U} = -\mathbf{G}\mathbf{V} \tag{1}$$

since $\mathbf{CG} = \mathbf{0}$ holds for every complex $\mathcal{K}$.

Moreover, Gauss' law and the current continuity law can be written in the discrete setting [10] as the following algebraic constraints:

$$-\mathbf{G}^T\mathbf{\Psi} = \mathbf{Q} \tag{2}$$

$$-\mathbf{G}^T\mathbf{I} = -i\omega\mathbf{Q} \tag{3}$$

respectively.

To form the final system of equations, discrete counterparts of *constitutive relations* must be added to the physical laws (1), (2), and (3). The discrete counterpart of the continuous electric constitutive relation $\mathrm{D} = \varepsilon\,\mathrm{E}$, where $\varepsilon$ is the positive definite permittivity tensor rewrites as

$$\mathbf{\Psi} = \mathbf{E}\mathbf{U} \tag{4}$$

where $\mathbf{E}$ is a symmetric positive definite square matrix of order $E$ linking the arrays $\mathbf{\Psi}$, $\mathbf{U}$. Similarly

$$\mathbf{I} = \mathbf{S}\mathbf{U} \tag{5}$$

is a discrete counterpart of the $\mathrm{J} = \sigma\,\mathrm{E}$ Ohm's constitutive relation, with $\sigma$ being the symmetric and positive definite conductivity tensor; the matrix $\mathbf{S}$ is symmetric positive definite and it links the arrays $\mathbf{I}$, $\mathbf{U}$. We observe that the matrices $\mathbf{E}$, $\mathbf{S}$ have the same geometric structure, since they map DoFs on primal edges to DoFs on dual faces. Therefore, they can be constructed efficiently with a single piece of software provided that permittivity is swap round with conductivity [10].

By combining (1), (4), (5), and (2) in (3), the following algebraic linear system of equations, having the scalar potentials $(\mathbf{V})_n$ in the nodes $n \in \mathcal{K}$ as unknowns, is obtained [10]

$$\left(\mathbf{G}^T\mathbf{S}\mathbf{G} + i\omega\mathbf{G}^T\mathbf{E}\mathbf{G}\right)\mathbf{V} = \mathbf{K}\,\mathbf{V} = \mathbf{0}. \tag{6}$$

In the following, we will propose an efficient method to construct the $\mathbf{K}$ matrix directly without passing through the construction of the single matrices $\mathbf{E}$, $\mathbf{S}$.

### A. *Efficient Computation of* $\mathbf{K}$

The geometric approach we pursue leads to an efficient computation of the stiffness matrix in terms of the geometric entities of the primal cell complex only [11]. In the following, without loosing generality, we focus on a single tetrahedron $v_k$ of the primal complex. With respect to $v_k$, we compute local $(\mathbf{K})^k$ matrix, with $k = 1, \ldots, V$; the corresponding global matrix $\mathbf{K}$ is easily deduced, by adding the local contributions from each tetrahedron of the complex, according to a standard assembling

[1] A vector field X is denoted in roman type.

[2] An array $\mathbf{X}$ is denoted in boldface type and its $i$th element reads $\mathbf{X}_i$.

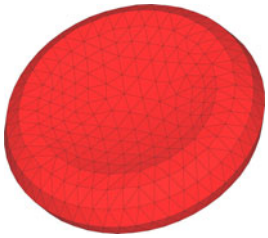

Fig. 2. Membrane of an erythrocyte represented by a triangular mesh.

process. The entry $(\mathbf{K})_{ij}^{k}$ of a local symmetric stiffness matrix for tetrahedron $v_k$, is given by

$$(\mathbf{K})_{ij}^{k} = \frac{1}{9|v_k|} D_{ki}\mathrm{f}_i \cdot (\sigma + i\omega\varepsilon)\; D_{kj}\mathrm{f}_j,\;\; \{i,j\} \in \{1,\ldots,4\} \tag{7}$$

where $\mathrm{f}_j$ denotes the area vector[3] of face $f_j$ opposite to node $n_j$, $|v_k|$ is the volume of the tetrahedron $v_k$, and $D_{ki}$ is the incidence between the pair $(v_k, f_i)$.

We note that the dual complex and incidence matrices are not explicitly constructed; in this way, they do not represent an overhead with respect to classical finite elements.

## III. Cell Membrane Modeling

In this section, we model thin layered structures, such as cell membranes, by means of the DGA for EQS; to this aim, we assume that the thin layer has a thickness of $\delta$ and its conductivity and permittivity are $\sigma_\delta$ and $\varepsilon_\delta$, respectively. Both conductivity and permittivity are assumed element-wise uniform.

In the case of thin layered structures, it is convenient not to mesh the thin layer with a 3-D mesh, since such layered structures are thousands of times thinner than the dimensions of the other objects in the domain of interest. Therefore, we will consider the layered structure as a surface with a 2-D triangular mesh on it; this allows us to reduce considerably the number of elements improving also the shape of the tetrahedra around the layered structure, which in turn allows us to reduce the discretisation error. As an example, in Fig. 2, such a triangulated surface $\mathcal{M}$ representing the membrane of an erythrocyte is shown.

### A. Geometric Formulation for the Thin Layer

The nodes belonging to $\mathcal{M}$ are doubled in such a way that a discontinuity of the electric scalar potential is allowed through the membrane [see Fig. 3(a)]. Each pair of nodes on $\mathcal{M}$, such as $\{n_i, n_j\}$ in Fig. 3(a), possesses the same coordinates but they are considered as two different elements of the simplicial complex $\mathcal{K}$. After updating the incidence matrices, the resulting new simplicial complex $\mathcal{K}'$ is not connected anymore.

Let us introduce an additional dual face on the membrane surface $\mathcal{M}$ for each node belonging to a node pair [see Fig. 3(b)]; we denote with $\tilde{f}_i$ the dual face pairing with node $n_i$ and $\tilde{f}_j$ the dual face pairing with node $n_j$. Each portion of $\tilde{f}_i$ [a quadrilateral surface, Fig. 3(b)] is tailored within a triangle of the cluster

[3]It is the vector having as amplitude the area of the face, normal to the face and oriented in a congruent way as the orientation of the face.

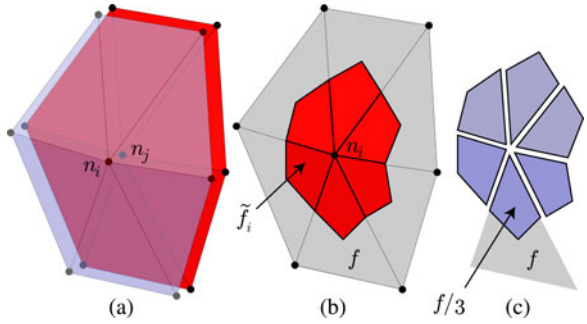


Fig. 3. (a) Nodes beloning to the membrane $\mathcal{M}$ are doubled. In this picture, the pairs of nodes, as $\{n_i, n_j\}$, are displayed one apart from the other only for clarity. In the membrane model, the nodes of a pair share exactly the same coordinates, so the nodes $\{n_i, n_j\}$ in the picture should be thought to be placed in the same point of the space. (b) Additional dual face $\tilde{f}_i$, dual to node $n_i$ in $\mathcal{M}$. Again, $\tilde{f}_i$ and $\tilde{f}_j$ relative to a node pair $\{n_i, n_j\}$ are coincident in terms of coordinates. (c) Quadrangles used to compute the thin layer equivalent admittances; the quadrilateral surface corresponding to $f$ has an area of $|f|/3$.

of triangles having $n_i$ in common; $\tilde{f}_j$ is obtained by duplicating $\tilde{f}_i$. We remark that $\tilde{f}_i$ and $\tilde{f}_j$ are stacked one over the other in such a way that they are coincident in terms of coordinates. Therefore, they, by no means, represent the boundary of a volumetric model of the membrane and there is no displacement between $\tilde{f}_i$ and $\tilde{f}_j$.

We define a *complex current* $I_{ij}$ entering $\tilde{f}_i$ and leaving $\tilde{f}_j$ thanks to the standard assumption that the current density is orthogonal to the membrane. Next, the equivalent admittance $\mathbf{Y}_{ij}^{s}$ of the thin layer associated with the pair of nodes $\{n_i, n_j\}$, relates the TMP difference $\mathbf{V}_i - \mathbf{V}_j$ corresponding to the nodes $\{n_i, n_j\}$ to the current $I_{ij}$ as

$$I_{ij} = \mathbf{Y}_{ij}^{s}\left(\mathbf{V}_i - \mathbf{V}_j\right). \tag{8}$$

To compute the equivalent admittance, we first obtain the per-unit-area admittance of the membrane assumed piecewise uniform in each triangle $f$ belonging to $\mathcal{M}$ as

$$\mathbf{S}_f^{s} = \frac{\sigma_\delta + i\omega\varepsilon_\delta}{\delta}. \tag{9}$$

Then, the $\mathbf{Y}_{ij}^{s}$ is computed by summing up all the admittances of the star of quadrangles around the node $n_i$ [see Fig. 3(c)] forming the additional dual faces $\tilde{f}_i$; this corresponds to the parallel of the admittances associated with each quadrangle. Since the area of the quadrilateral surface tailored within triangle $f$ of $\mathcal{M}$ is $|f|/3$, then the equivalent admittance becomes

$$\mathbf{Y}_{ij}^{s} = \sum_{f \in \mathcal{C}_i} \frac{|f|}{3} \mathbf{S}_f^{s} \tag{10}$$

where $\mathcal{C}_i$ is the cluster of triangles $f$ having the node $n_i$ in common. We collect the equivalent admittances of all thin layers in the array $\mathbf{Y}^{s}$.

### B. Modified System of Equations

Now, we need to couple the currents $I_{ij}$ from (8) for all the pairs $\{n_i, n_j\}$ in the layer $\mathcal{M}$ with system (6). To this aim, we consider the dual volumes $\tilde{v}_i$ and $\tilde{v}_j$ on the two sides of the

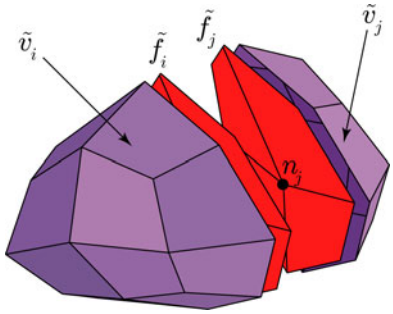


Fig. 4. Exploded view of the two dual volumes $\tilde{v}_i, \tilde{v}_j$ dual to the pair of nodes $\{n_i, n_j\} \in \mathcal{M}$. The two dual volumes have the additional dual faces $\tilde{f}_i$, $\tilde{f}_j$, respectively, in their boundaries.

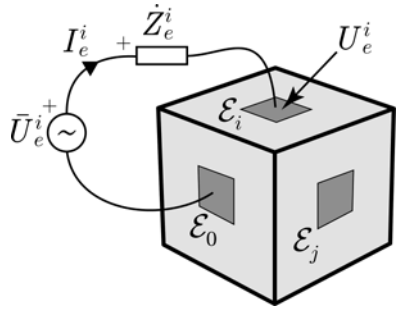


Fig. 5. Contact impedance $\dot{Z}_e^i$ in series to the $i$th electrode.

layer $\mathcal{M}$, refer to Fig. 4. The dual volume $\tilde{v}_i$ is dual to the node $n_i \in \mathcal{M}$ and the other, $\tilde{v}_j$, is dual to $n_j \in \mathcal{M}$. It is apparent that dual faces $\tilde{f}_i, \tilde{f}_j$ complete the boundaries of $\tilde{v}_i, \tilde{v}_j$, respectively, and $I_{ij}$ is the current on $\tilde{f}_i$ while $-I_{ij}$ is the complex current on $\tilde{f}_j$ since $\tilde{v}_i, \tilde{v}_j$ are oriented by the respective outer normals; then, the balance laws (2), (3) applied to the boundaries of $\tilde{v}_i$, $\tilde{v}_j$, together with (1), (4), and (5), modify (6) as

$$(\mathbf{KV})_i + I_{ij} = (\mathbf{KV})_i + \mathbf{Y}_{ij}^s (\mathbf{V}_i - \mathbf{V}_j) = 0$$
$$(\mathbf{KV})_j - I_{ij} = (\mathbf{KV})_j - \mathbf{Y}_{ij}^s (\mathbf{V}_i - \mathbf{V}_j) = 0$$

where we used (8) for $I_{ij} \quad \forall \{n_i, n_j\} \in \mathcal{M}$.

### C. Implementation of the Membrane Model

We summarize the practical steps for implementing the novel membrane model.

1) The complex $\mathcal{K}'$ can be generated in the preprocessing step in various ways. One may construct the mesh for each biological cell independently. Then, the mesh of the extracellular medium has to be constructed taking care that the nodes and triangles on the interfaces between the cell meshes and the extracellular medium mesh have to match. This operation is possible with most mesh generators as TETGEN (available at http://www.tetgen.org).

   Another solution, used in our implementation, is to mesh the entire domain as usual with the complex $\mathcal{K}$. Then, cycle each node and see if it lies on a membrane. If so, then add a new node at the bottom of the node list with the same coordinates as the original node. An array may be used to keep track of the correspondence related to the node pairs (i.e., for the node pair $\{n_i, n_j\}$, the array should return the integer label of $n_j$ given the label of $n_i$ as input with $j = \mathrm{nodepair}(i)$). The last step is to cycle each volume $v$ and see if it is inside a biological cell or outside. If it is outside, nothing is done and the original labels of the nodes of $v$ are kept. If it is inside, cycle each node $n$ of the four nodes incident to $v$. If $\mathrm{nodepair}(n)$ is nonzero, then update the incidence of $v$ with respect to $n$ with $\mathrm{incidence}(v, n) = \mathrm{nodepair}(\mathrm{incidence}(v, n))$.
2) Cycling the triangles on the membranes, construct by assembling the entries of the array $\mathbf{Y}^s$ that are initially set to zero. Namely, for a generic face $f \in \mathcal{M}$, assemble in the array the following contributions
   a) $\mathbf{Y}_{ij}^s = \mathbf{Y}_{ij}^s + \mathbf{S}_f^s |f|/3$
   b) $\mathbf{Y}_{hk}^s = \mathbf{Y}_{hk}^s + \mathbf{S}_f^s |f|/3$
   c) $\mathbf{Y}_{vz}^s = \mathbf{Y}_{vz}^s + \mathbf{S}_f^s |f|/3$

   where $\{n_i, n_j\}, \{n_h, n_k\}$, and $\{n_v, n_z\}$ are the three node pairs of the face $f$.
3) Starting from the usual sparse matrix $\mathbf{K}$ in (6), without taking into account the membranes, assemble for each pair of doubled nodes $\{n_i, n_j\}$ the values
   a) $(\mathbf{K})_{ii} = (\mathbf{K})_{ii} + \mathbf{Y}_{ij}^s$
   b) $(\mathbf{K})_{jj} = (\mathbf{K})_{jj} + \mathbf{Y}_{ij}^s$
   c) $(\mathbf{K})_{ij} = (\mathbf{K})_{ij} - \mathbf{Y}_{ij}^s$
   d) $(\mathbf{K})_{ji} = (\mathbf{K})_{ji} - \mathbf{Y}_{ij}^s$.

## IV. Boundary Conditions and Electrode Contact Impedance Modeling

A number $N_e + 1$ of electrodes $\{\mathcal{E}_i\}_{i=0}^{N_e}$ is defined, which are by hypothesis disjoint and equipotential surfaces each; we denote with $\mathcal{E}_0$ the reference electrode. On this set, a Dirichlet boundary condition is applied. In the complement of $\partial\mathcal{K}$ with respect to the union of the electrode surfaces, a homogeneous Neumann boundary condition is imposed.

There are three typical ways to enforce a consistent excitation for each electrode (see Fig. 5). i) The potential difference $U_e^i = \bar{U}_e^i$ of the $i$th electrode with respect to the reference electrode is prescribed. This happens in practice when an e.m.f. generator $\bar{U}_e^i$ is connected between the $i$th and the reference electrode. The result is that the potential is fixed (and known) while the total electric current $I_e^i$ flowing through the $i$th electrode can be determined by solving (6).

ii) The current flowing through the electrode is prescribed. This is the dual case of the 1); this time the potential is not fixed and can "float" [a typical informal expression equivalent to say that the potential is not fixed but it is determined by solving (6)]. This motivates the reason why this kind of condition is called a *floating potential constraint*.[4] Finally, the third case iii) is analogous to i) but deals with the presence of a *contact impedance* $\dot{Z}_e^i$ placed in series between the electric generator and the considered electrode (see Fig. 5). In this case, as we

[4]Frequently, the current specified is zero. This corresponds to model a conductor which is not connected to any electric generator.

are going to see in detail, both the total current and voltage are unknowns and have to be determined by solving (6).

### A. Formulation of the Linear System

Let us order the electrodes in such a way that the first $N$ have a potential difference $U_e^i = \bar{U}_e^i$ fixed, this corresponds to the case i); electrodes from $N+1$ to $H$ have a current $I_e^i = \bar{I}_e^i$ fixed, this corresponds to the case ii); finally, electrodes from $H+1$ to $N_e$ have a known contact impedance in series as in the case iii). Let us order the node's labels in such a way that the nodes $n \in \mathcal{K} \setminus \bigcup_{i=0}^{N_e} \mathcal{E}_i$ come first; they are referred to as *interior nodes* and are collected in a subarray $\mathbf{V}'$. Next, come the nodes $n \in \bigcup_{j=0}^{N} \mathcal{E}_j$, $n \in \bigcup_{k=N+1}^{H} \mathcal{E}_k$, $n \in \bigcup_{k=H+1}^{N_e} \mathcal{E}_k$, respectively. Consequently, the array $\mathbf{V}$ is correspondingly partitioned into four subarrays $\mathbf{V}'$, $\bar{\mathbf{V}}$, $\mathbf{V}''$, and $\mathbf{V}'''$. Partitioning also the matrix $\mathbf{K}$, the linear system of equations (6) can be written as

$$\begin{bmatrix} \mathbf{K}_{11} & \mathbf{K}_{12} & \mathbf{K}_{13} & \mathbf{K}_{14} \\ \mathbf{K}_{21} & \mathbf{K}_{22} & \mathbf{K}_{23} & \mathbf{K}_{24} \\ \mathbf{K}_{31} & \mathbf{K}_{32} & \mathbf{K}_{33} & \mathbf{K}_{34} \\ \mathbf{K}_{41} & \mathbf{K}_{42} & \mathbf{K}_{43} & \mathbf{K}_{44} \end{bmatrix} \begin{bmatrix} \mathbf{V}' \\ \bar{\mathbf{V}} \\ \mathbf{V}'' \\ \mathbf{V}''' \end{bmatrix} = \begin{bmatrix} \mathbf{0} \\ \mathbf{I}_s \\ \mathbf{I}_s'' \\ \mathbf{I}_s''' \end{bmatrix} \tag{11}$$

where $\mathbf{I}_s$, $\mathbf{I}_s''$, and $\mathbf{I}_s'''$ are unknown currents.

We note that when dealing with practical meshes, each pair of electrodes is separated by much more than two layers of mesh elements. This implies[5] that there is no coupling term between electrodes so $\mathbf{K}_{23} = \mathbf{0}$, $\mathbf{K}_{24} = \mathbf{0}$, $\mathbf{K}_{32} = \mathbf{0}$, $\mathbf{K}_{34} = \mathbf{0}$, $\mathbf{K}_{42} = \mathbf{0}$, and $\mathbf{K}_{43} = \mathbf{0}$. The system can be rewritten as

$$\begin{bmatrix} \mathbf{K}_{11} & \mathbf{K}_{12} & \mathbf{K}_{13} & \mathbf{K}_{14} \\ \mathbf{K}_{21} & \mathbf{K}_{22} & \mathbf{0} & \mathbf{0} \\ \mathbf{K}_{31} & \mathbf{0} & \mathbf{K}_{33} & \mathbf{0} \\ \mathbf{K}_{41} & \mathbf{0} & \mathbf{0} & \mathbf{K}_{44} \end{bmatrix} \begin{bmatrix} \mathbf{V}' \\ \bar{\mathbf{V}} \\ \mathbf{V}'' \\ \mathbf{V}''' \end{bmatrix} = \begin{bmatrix} \mathbf{0} \\ \mathbf{I}_s \\ \mathbf{I}_s'' \\ \mathbf{I}_s''' \end{bmatrix}. \tag{12}$$

Next, we introduce the arrays $\mathbf{n}^i$ for $i \in \{0, \ldots, N\}$ as

$$\begin{aligned} \mathbf{n}_n^i &= 1 \quad \forall n \in \mathcal{E}_i \\ \mathbf{n}_n^i &= 0 \quad \forall n \in \bigcup_{j=0, j\neq i}^{N} \mathcal{E}_j; \end{aligned} \tag{13}$$

for $i \in \{N+1, \ldots, H\}$ as

$$\begin{aligned} \mathbf{n}_n^i &= 1 \quad \forall n \in \mathcal{E}_i \\ \mathbf{n}_n^i &= 0 \quad \forall n \in \bigcup_{k=N+1, k\neq i}^{H} \mathcal{E}_k; \end{aligned} \tag{14}$$

for $i \in \{H+1, \ldots, N_e\}$ as

$$\begin{aligned} \mathbf{n}_n^i &= 1 \quad \forall n \in \mathcal{E}_i \\ \mathbf{n}_n^i &= 0 \quad \forall n \in \bigcup_{k=H+1, k\neq i}^{N_e} \mathcal{E}_k. \end{aligned} \tag{15}$$

Thanks to the Dirichlet boundary condition, the three arrays $\bar{\mathbf{V}}$, $\mathbf{V}''$, and $\mathbf{V}'''$ can be written in terms of the electrodes potential differences $\{U_e^i\}, i \in \{1, \ldots, N_e\}$, as

$$\begin{aligned} \bar{\mathbf{V}} &= \sum_{j=1}^{N} \bar{U}_e^j \, \mathbf{n}^j, \qquad \mathbf{V}'' = \sum_{k=N+1}^{H} U_e^k \, \mathbf{n}^k \\ \mathbf{V}''' &= \sum_{k=H+1}^{N_e} U_e^k \, \mathbf{n}^k. \end{aligned} \tag{16}$$

Substituting (16) inside (12), we can consider as unknowns the $\{U_e^i\}_{i=N+1}^{N_e}$ in place of the DoFs belonging to the arrays $\mathbf{V}''$ and $\mathbf{V}'''$. Moving the known terms resulting from $\bar{\mathbf{V}}$ on the right-hand side, it is easy to see that the final equations for the interior nodes become

$$\mathbf{K}_{11} \, \mathbf{V}' + \mathbf{K}_{13} \, \mathbf{n}'' \, \mathbf{U}_e'' + \mathbf{K}_{14} \, \mathbf{n}''' \, \mathbf{U}_e''' = -\mathbf{K}_{12} \, \bar{\mathbf{n}} \, \bar{\mathbf{U}}_e \tag{17}$$

where we introduce the array $\bar{\mathbf{U}}_e = \{U_e^1, \ldots, U_e^N\}^T$, $\mathbf{U}_e'' = \{U_e^{N+1}, \ldots, U_e^H\}^T$, $\mathbf{U}_e''' = \{U_e^{H+1}, \ldots, U_e^{N_e}\}^T$ and the matrices $\bar{\mathbf{n}} = \{\mathbf{n}^1, \mathbf{n}^2, \ldots, \mathbf{n}^N\}$, $\mathbf{n}'' = \{\mathbf{n}^{N+1}, \ldots, \mathbf{n}^H\}$, $\mathbf{n}''' = \{\mathbf{n}^{H+1}, \ldots, \mathbf{n}^{N_e}\}$.

Equation (17) has more unknowns than equations. One equation for each floating potential electrode should be added to specify the current flowing through it. This equation is a *nonlocal algebraic current continuity law* [8] obtained by summing up[6] all local continuity laws relative to each node belonging to the considered electrode as

$$\left(\mathbf{n}^{k\,T} \, \mathbf{K}_{31}\right) \mathbf{V}' + \left(\mathbf{n}^{k\,T} \, \mathbf{K}_{33} \, \mathbf{n}^k\right) U_e^k = I_e^k \tag{18}$$

for $k \in \{N+1, \ldots, H\}$ and

$$\left(\mathbf{n}^{j\,T} \, \mathbf{K}_{41}\right) \mathbf{V}' + \left(\mathbf{n}^{j\,T} \, \mathbf{K}_{44} \, \mathbf{n}^j\right) U_e^j - I_e^j = 0 \tag{19}$$

for $j \in \{H+1, \ldots, N_e\}$.

Still, we miss one equation for each current unknown $\{I_e^j\}_{j=H+1}^{N_e}$. The missing equations stem from Kirchhoff's laws needed to take into account the contact impedances $\dot{Z}_e^j$ and the e.m.f.s in series $\bar{U}_e^j$, see Fig. 5.

$$\bar{U}_e^j - U_e^j = \dot{Z}_e^j \, I_e^j, \;\; j \in \{H+1, \ldots, N_e\}.$$

This equation can be rewritten as

$$-U_e^j - \dot{Z}_e^j \, I_e^j = -\bar{U}_e^j, \;\; j \in \{H+1, \ldots, N_e\}. \tag{20}$$

Then, (17), together with (18), (19), and (20), form the final symmetric linear system of equations.

## V. Numerical Results

The formulation described in this paper has been integrated into the Geometric Approach to Maxwell's Equations (GAME) research code [14]. The software has been implemented in Fortran 90 and the Intel Fortran 90 Compiler has been used to produce the executable. The PARDISO direct solver contained in the Intel MKL scientific library has been employed to solve the resulting linear system of equations. The hardware used for

[5]The interaction between a node $n$ is limited to the nodes belonging to the cluster of tetrahedra of around $n$.

[6]This correspond to apply a current continuity law on a surface which "encircles" the considered electrode.

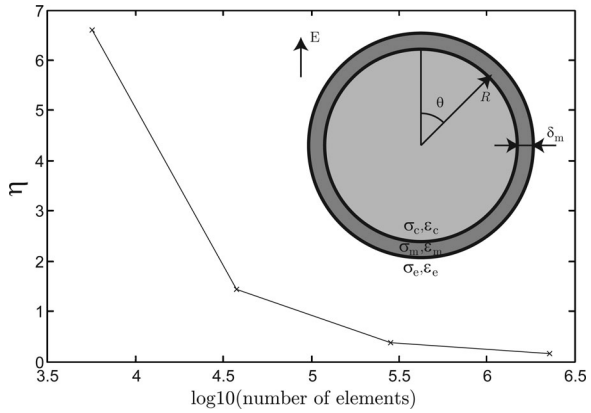


Fig. 6. Spherical cell with a membrane in a uniform EQS field. Convergence of the maximum error on the transmembrane voltage with mesh refinement for the spherical cell benchmark.

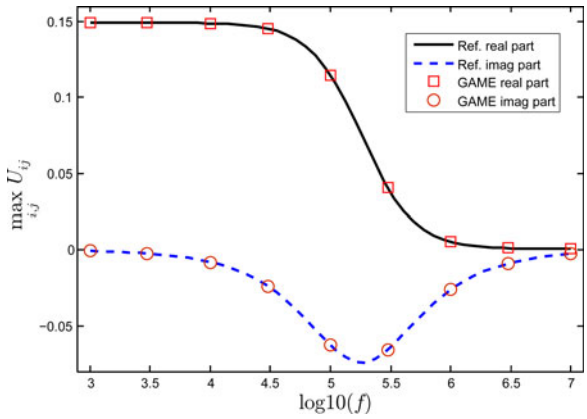


Fig. 7. Frequency behavior of the transmembrane voltage for the spherical cell benchmark.

the computations consists of an Intel Core 2 Duo T7700 2.4GHz laptop with 4GB of RAM.

In the following, the code is validated against an analytical solution and on experimental data.

### A. Code Validation

To validate the results produced by the described formulation, a spherical cell with a radius $R = 10\,\mu$m has been considered (see Fig. 6). The cell possesses a membrane with a conductivity $\sigma_m = 5 \cdot 10^{-7}\,\mathrm{S/m}$ and a thickness $\delta_m = 5$ nm. The extracellular conductivity has been set to $\sigma_e = 1$ S/m, whereas the cytoplasmatic conductivity has been set to $\sigma_c = 0.2\,\mathrm{S/m}$. The cell is placed in a region with a static and uniform electric field with a modulus of $100\,\mathrm{V/cm}$.

The transmembrane voltage is computed as $U_{ij} = \mathbf{V}_i - \mathbf{V}_j$, for all pairs of doubled nodes $\{i, j\}$. The error on the transmembrane voltage is computed as $\epsilon_{ij} = |U_{ij} - U_{ij}^{\mathrm{ref}}|$, where $U_{ij}^{\mathrm{ref}}$ is the analytical value of the TMP in one of the nodes $\{i, j\}$ provided by the Schwan equation [2], [12]. The convergence with mesh refinement of $\eta = 100\,\max_{i,j}(\epsilon_{ij})/U_{hk}^{\mathrm{ref}}$, where $\{h, k\} = \arg\max_{i,j}(\epsilon_{ij})$, is depicted in Fig. 6.

Then, an EQS problem has been solved by considering the cell placed in a uniform ac field with a modulus of 100 V/cm. A relative permittivity of $\varepsilon_{re} = 80$, $\varepsilon_{rc} = 80$, and $\varepsilon_{rm} = 9$ has been assumed for the extracellular medium, cytoplasm, and membrane, respectively. In Fig. 7, we compare with the analytical solution [13], the modulus of the maximum transmembrane voltage at frequencies ranging from 1 kHz to 10 MHz.

### B. Experimental Results With Whole Blood

As a second experimental benchmark, whole blood with physiological hematocrit (46%) flowing in a microchannel at a high shear rate ($3000\ \mathrm{s}^{-1}$) has been considered. It is known that red blood cells (RBC) suspensions in a quiescent state tend to aggregate in pillars (so-called rouleaux). RBC aggregates start to disappear at low shear rates. At high shear rates, RBCs tend to deform into prolate ellipsoids with their long axis aligned parallel to the flow, and form layers that slide on adjacent plasma layers [15]–[17].

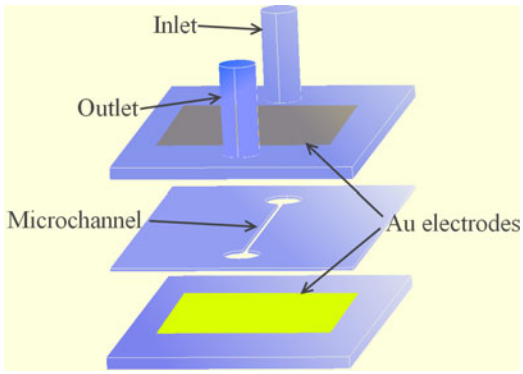


Fig. 8. Sensing device exploded drawing. Microchannel dimensions are $25 \times 0.4 \times 0.25$ mm.

The measurement bench is composed by a sensing device and a high-accuracy *LCR* meter, the Agilent HP E4980a. The sensing device, as shown in Fig. 8, is composed by three assembled layers which are kept together by fasteners. The upper layer in Fig. 8 is a 2-mm thick polycarbonate slide where microfluidic couplers are bonded and, on its bottom, a 180-nm thick gold electrode has been sputtered; the electrode dimensions are 25 mm in length and 15 mm in width. The middle layer is a 250-$\mu$m thick dimethyl-siloxane membrane where a 25-mm long and 400-$\mu$m wide microchannel is etched. The lower layer is another 2-mm thick polycarbonate slide where a second gold electrode (identical in dimensions to the upper one) has been sputtered. The resulting assembled geometry is a $25 \times 0.4 \times 0.25$ mm rectangular duct having as top and bottom walls the gold electrodes.

The measurements have been performed in a two-wires configuration with a 0.1-V ac voltage in the frequency range 1 kHz–2 MHz, ten points on the whole range logarithmically spaced; the driving voltage amplitude has been set as low as 0.1 V in order to avoid redox reactions between gold electrodes and electrolytes dissolved in plasma. In order to increase the accuracy of the measurements, a short/open calibration of

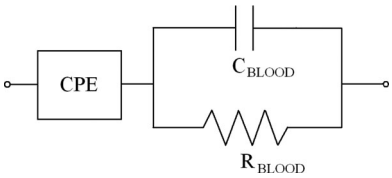


Fig. 9. Equivalent circuit for impedance measurements on blood: CPE models the double layer phenomenon while $C_{\mathrm{BLOOD}}$ and $R_{\mathrm{BLOOD}}$ model blood impedance.

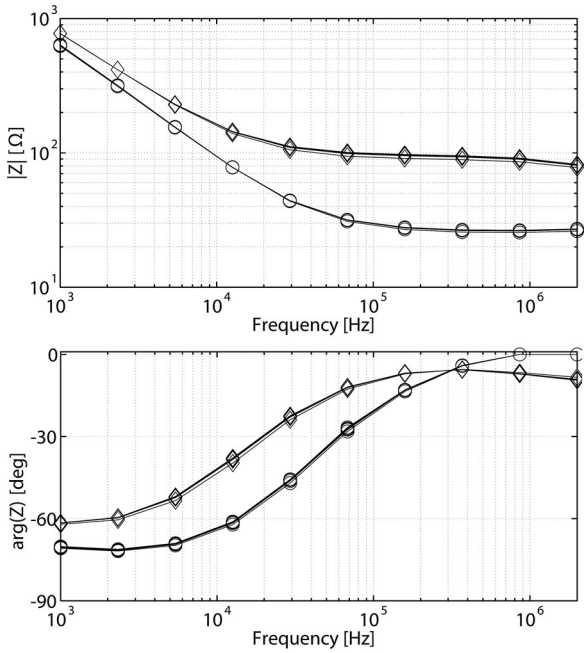


Fig. 10. Measured impedance (in amplitude and phase) and its repeatability during flow are shown; symbol ◯ denotes plasma while ◇ indicates the whole blood.

the instrument with the same cables connected to the sensing device has been performed; this yields to an impedance accuracy of 0.1% in magnitude and phase [20].

It is well known in Impedance Spectroscopy theory [21] that the interaction between a metal electrode and a fluid, wherein salts are dissolved, gives rise to the phenomenon of a double charge layer (*double layer*); this phenomenon can be modeled as a constant phase element CPE in series to the measurand

$$Z_{\mathrm{CPE}} = \frac{1}{C(j\omega)^{\alpha}} \tag{21}$$

where $0 \leq \alpha \leq 1$ in (21) is the phase shift of the CPE.

In order to well discern the double layer contribution from the measurand, the frequency span has been set quite wide to fit the data with an interpolation software which can provide (given a known circuital model) the parameters of the model. In Fig. 9, it is shown the equivalent circuit for blood and plasma; it takes into account the double layer, the blood resistance, and the blood capacitance.

Impedance data have been acquired from the same patient's plasma and blood, before and after centrifugation. In Fig. 10, it is shown the impedance behavior in terms of magnitude and

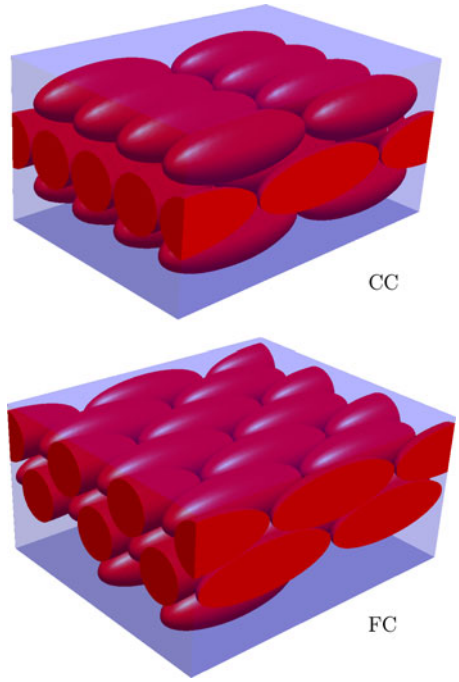


Fig. 11. Model of RBCs suspension with cells arranged in a cell centered (CC) or face centered (FC) cubic lattice.

phase of plasma and blood; as a repeatability estimation plasma and blood have flown inside the microchannel for 5 min and data have been acquired every 2 s. Repeatability data showed a measurement accuracy always within 0.3% and in Fig. 10 only few curves (for graphical reasons) acquired every 20 s are shown. As can be seen, the double layer plays an important role at low frequencies while at higher frequencies the impedance is mainly resistive. The impedance value at high frequencies is 27 Ω for plasma and 90 Ω for blood; this yields, known the microchannel geometry, to a conductivity of plasma $\sigma_{\mathrm{PLASMA}} \simeq 0.9\ \mathrm{S/m}$ and a conductivity of blood $\sigma_{\mathrm{BLOOD}} \simeq 0.27\ \mathrm{S/m}$; these data are also in accordance with the Maxwell–Fricke relation [18], [19]

$$\frac{\sigma_{\mathrm{BLOOD}}}{\sigma_{\mathrm{PLASMA}}} = \frac{1-H}{1+(C-1)H} \tag{22}$$

where $H$ is the hematocrit content and $C$ is a geometrical factor depending on RBCs mean orientation with respect to the direction of the electric field. Since in this case $H = 0.46$, fits the measured data ($\sigma_{\mathrm{BLOOD}}/\sigma_{\mathrm{PLASMA}} \simeq 0.3$) when $C \simeq 2.74$; this means that RBCs orientation is mainly along the axis of the flow as it is certainly the case thanks to the high shear rate. The ratio of the major and minor semiaxes of the prolate ellipsoid is close to 3. In the RBCs layers that form in a flow with high shear rate, RBCs are necessarily tightly packed since the RBCs density in the layers is much greater than the haematocrit, which notoriously is defined as the average RBCs density in the entire volume. This justifies the assumption of arranging the RBCs in a quasi-lattice, which presents a high packing density. For this reasons, the simulations have been performed by considering a suspension of RBCs ordered in a cell centered (CC) or face centered (FC) cubic quasi-lattice as shown in Fig. 11. The bottom plane of the simulated regions has been

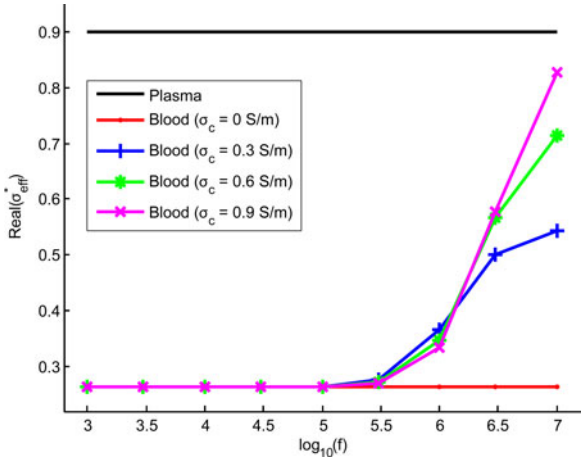


Fig. 12. Variation of the real part of the effective complex conductivity versus frequency and conductivity of the cytoplasm.

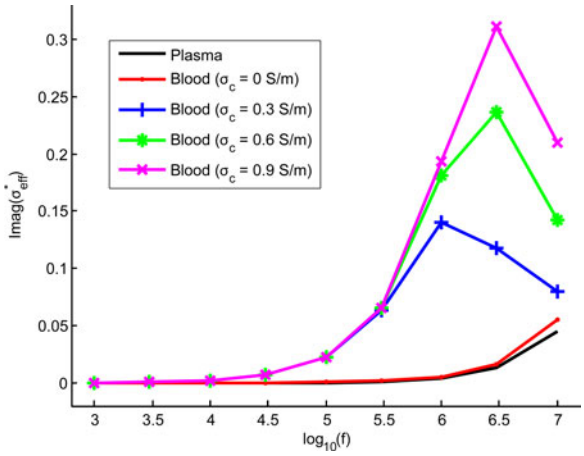


Fig. 13. Variation of the imaginary part of the effective complex conductivity versus frequency and conductivity of the cytoplasm.

set to ground (i.e., a homogeneous Dirichlet boundary condition), while the top plane is connected to an electric generator through a contact impedance. A symmetry condition is considered on the lateral sides by means of a homogeneous Neumann boundary condition. The ellipsoids have the major semiaxis of 6 $\mu$m and a minor semiaxis of 2 $\mu$m. This gives the patient RBC mean volume (MCV) of about 100 $\mu$m$^3$. The conductivity and relative permittivity of plasma are set to $\sigma_{\mathrm{PLASMA}} = 0.9$ S/m and $\varepsilon_{r\mathrm{PLASMA}} = 90$, of membrane to $\sigma_m = 5 \cdot 10^{-7}$ S/m and $\varepsilon_{rm} = 9$ and of cytoplasm to $\sigma_c = 0.3$ S/m and $\varepsilon_{rc} = 60$. The thickness of the membrane is 5 nm. The simulations provide 0.298 and 0.293 ratios of conductivity $\sigma_{\mathrm{BLOOD}}/\sigma_{\mathrm{PLASMA}}$ for CC and FC lattices, respectively; such results are in a very good agreement with the Maxwell–Fricke theory, which assumes the RBCs as insulators.

We introduce the effective complex conductivity $\sigma^*_{\mathrm{eff}} = \frac{I^1_e}{U^1_e}\frac{L_{\mathrm{box}}}{S_{\mathrm{box}}}$, where $L_{\mathrm{box}}$ and $S_{\mathrm{box}}$ are the height and the area of the base of the simulated regions, respectively. In order to estimate the impact of the cytoplasmatic conductivity, that may be strongly patient specific, on $\sigma^*_{\mathrm{eff}}$, various conductivities of the cytoplasm ranging from zero to the conductivity of the plasma have been considered. This allows us to test the variability of $\sigma^*_{\mathrm{eff}}$ with respect to the cytoplasmatic conductivity and to explore the behavior of the system at frequencies that at the present state cannot be analyzed with our measurement bench. The results versus frequency are shown in Figs. 12 and 13. No significative differences have been reported for the CC or FC lattices.

## VI. Conclusion

This paper presented a geometric approach to model cell membranes and electrodes contact impedances in a way close to the governing physical phenomena. The first advantage is that the linear system entries, and, in particular, their contributions due to the presence of the membranes are geometrically defined and can be computed in a closed form without the need of any numerical integration. Moreover, the global current associated with the surface of each electrode is obtained directly without any numerical integration. The method proposed in this paper may be used for modeling suspension of cells for bioelectromagnetics research, for example, dosimetry for electroporation and optimization of lab-on-a-chip devices, especially for problems too large to be simulated with commercial softwares.

## References

[1] P. E. Boukani, A. Morss, W.-C. Liao, B. Henslee, H.-C. Jung, X. Zhang, B. Yu, X. Wang, Y. Wu, L. Li, K. Gao, X. Hu, X. Zhao, O. Hemminger, W. Lu, G. P. Lafyatis, and L. James Le, "Nanochannel electroporation delivers precise amounts of biomolecules into living cells," *Nature Nanotechnol.*, vol. 6, pp. 747–754, 2011.

[2] G. Pucihar, T. Kotnik, B. Valič, and D. Miklavčič, "Numerical determination of transmembrane voltage induced on irregularly shaped cells," *Ann. Biomed. Eng.*, vol. 34, pp. 642–652, 2006.

[3] G. Pucihar, D. Miklavčič, and T. Kotnik, "A time-dependent numerical model of transmembrane voltage inducement and electroporation of irregularly shaped cells," *IEEE Trans. Biomed. Eng.*, vol. 56, no. 5, pp. 1491–1501, May 2009.

[4] C. E. Miller and C. S. Henriquez, "Three-dimensional finite element solution for biopotentials: Erythrocyte in an applied field," *IEEE Trans. Biomed. Eng.*, vol. 35, no. 9, pp. 712–718, Sep. 1988.

[5] I. Meny, N. Burais, F. Buret, and L. Nicolas, "Finite-Element modeling of cell exposed to harmonic and transient electric fields," *IEEE Trans. Magn.*, vol. 43, no. 4, pp. 1773–1776, 2007.

[6] E. Tonti. (1975). "On the formal structure of physical theories," Monograph of the Italian National Research Council. Available: http://www.dic.univ.trieste.it/perspage/tonti/DEPOSITO/CNR.pdf

[7] A. Bossavit, *Computational Electromagnetism*. Orlando, FL: Academic Press, 1998.

[8] P. Dłotko, R. Specogna, and F. Trevisan, "Automatic generation of cuts on large-sized meshes for the $T$-$\Omega$ geometric eddy-current formulation," *Comput. Methods Appl. Mech. Engrg.*, vol. 198, pp. 3765–3781, 2009.

[9] J. R. Munkres, *Elements of Algebraic Topology*. Cambridge, MA: Perseus Books, 1984.

[10] P. Bettini, R. Specogna, and F. Trevisan, "Electroquasistatic analysis of the gas insulated line for the ITER neutral beam injector," *IEEE Trans. Magn.*, vol. 45, no. 3, pp. 996–999, Mar. 2009.

[11] R. Specogna and F. Trevisan, "A discrete geometric approach to solving time independent Schrödinger equation," *J. Comput. Phys.*, vol. 230, pp. 1370–1381, 2011.

[12] H. P. Schwan, "Electrical properties of tissue and cell suspensions," *Adv. Biol. Med. Phys.*, vol. 5, pp. 147–209, 1957.

[13] T. Kotnik and D. Miklavčič, "Theoretical evaluation of the distributed power dissipation in biological cells exposed to electric fields," *Bioelectromagnetics*, vol. 21, pp. 385–394, 2000.

[14] R. Specogna and F. Trevisan, "GAME (Geometric Approach to Maxwell's Equations) code," Copyright 2003–2012.

[15] H. Schmid-Schonbein and R. Wells, "Fluid drop-like transition of erythrocytes under shear," *Science*, vol. 165, pp. 288–291, 1969.
[16] G. B. Thurston, "Plasma relase-cell layering theory for blood flow," *Biorheology*, vol. 26, pp. 199–214, 1989.
[17] G. B. Thurston, "Viscoelastic properties of blood and blood analogs," in *Advances in Haemodynamics and Hemorheology*. T. C. How, Ed. Greenwich, CN: JAI Press, 1996, pp. 1–30.
[18] H. Fricke, "A mathematical treatment of the electric conductivity and capacity of disperse systems I," *Phys. Rev.*, vol. 24, pp. 575–587, 1924.
[19] A. E. Hoetink, T. J. Faes, K. R. Visser, and R. M. Heethaar, "On the flow dependency of the electrical conductivity of blood," *IEEE Trans. Biomed. Eng.*, vol. 51, no. 7, pp. 1251–1261, Jul. 2004.
[20] *Agilent E4980A Precision LCR Meter Users Guide*,' 7th Edition, Agilent Technology, Santa Clara, CA, Manufacturing No. E4980-90070, Jun. 2008.
[21] E. Barsoukov and J. R. Macdonald, *Impedance Spectroscopy: Theory, Experiment and Applications*. New York: Wiley, 2005.

**Antonio Affanni** received the Master degree in electronic engineering from the University of Parma, Italy, in 2003 and the Ph.D. degree in 2007 in information technologies from the same University.

In 2009, he joined the Department of Electrical, Mechanical, and Management Engineering at the University of Udine, Udin, Italy, as Researcher. His research interests involve the design of sensors for industrial applications and the development of microfluidic sensors/actuators for biological applications.

**Ruben Specogna** (S'05–M'08) was born in Cividale del Friuli (UD), Italy, in 1977. He received the Master degree in electronic engineering and the Ph.D. degree in electrical engineering from the University of Udine, Udine, Italy, in 2003 and 2007, respectively.

From 2008, he is an Assistant Professor of Electromagnetic Compatibility and Electrical Science in the University of Udine. He is author of more than 45 papers in ISI scientific journals, mainly in the field of computational electromagnetism, coupled problems (MEMS and nanoelectronics), computational topology and computer aided design, nuclear fusion reactors engineering and design, and biosensors.

**Francesco Trevisan** was born in Treviso, Italy, in 1964. He graduated with honours in "Ingegneria Elettrotecnica" (Power Electrical Engineering) in 1988 from the University of Padova, Italy.

Since 1991, he has been Researcher at the Istituto Gas Ionizzati of the National Research Council in Padova working, with the "Magnet System" group, at the electromagnetic design of the experimental machine RFX (Reverse Field eXperiment) for research on magnetically confined nuclear fusion. In 1995, he joined, as researcher, in the Department of Electrical, Management and Mechanical Engineering, University of Udine, Italy, where from 2000, he is Associate Professor teaching "Numerical Models for Fields and Circuits." His research interests have been focused on the analysis, synthesis, and optimization of magnetic configurations in magnetically confined plasmas for fusion research and on the numerical formulations for the solution of Maxwell equations by means of the so called "Discrete Geometric Approach" from statics to wave propagation. In this topics he matured a solid scientific expertise, recognized at international level and documented by more than 110 scientific papers.